

**ORAL SESSION:
APPLICATIONS 2**

ASSESSMENT OF FUEL CELL'S CONTACT PRESSURE DISTRIBUTION BY MEANS OF DISTRIBUTED FILM SENSORS AND DIGITAL IMAGE CORRELATION TECHNIQUES

R. Montanini

Dipartimento di Chimica Industriale e Ingegneria dei Materiali, Università degli Studi di Messina, Salita Sperone 31, 98166 – Messina, Italy

G. Squadrito, G. Giacoppo

Istituto di Tecnologie Avanzate per l'Energia "Nicola Giordano", Salita Santa Lucia Sopra Contesse 5, 98126 – Messina, Italy

Abstract

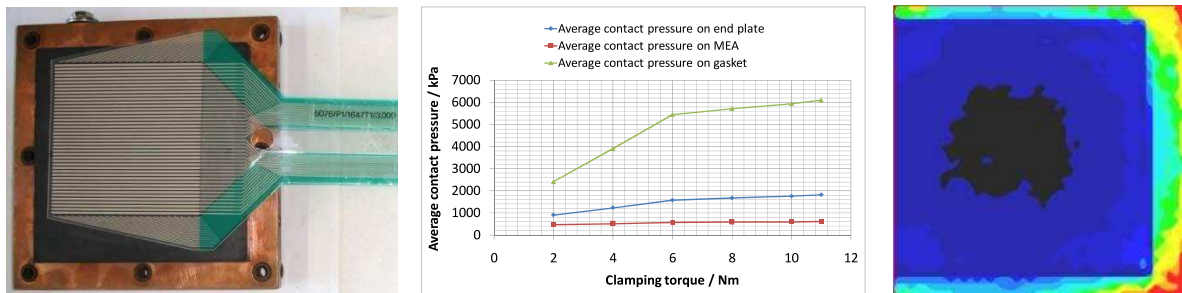
The achievement of a proper and uniform pressure distribution between the membrane electrode assembly (MEA) and the bipolar plates of a proton exchange membrane fuel cell (PEMFC) is a key factor of stack design and assembly. Uneven distribution of the contact pressure will result in hot spots which may have a detrimental effect on PEMFC electro-chemical performance and life. An insufficient clamping pressure may result in sealing problems, such as fuel leakage, internal crossover and high contact resistance between the gas diffusion layer (GDL) and the bipolar plates. On the other hand, a high clamping pressure may squeeze the relatively thin GDL and change its porosity and permeability, choking the flow of gases and making the migration of water difficult. Very little scientific research has been focused on the measurement of the contact pressure distribution within the fuel cell and its correlation with the applied clamping torque.

This study explores the possibility of using matrix-based piezoresistive thin-film sensors, to be placed between the MEA and the monopolar plate of a PEMFC, and digital image techniques to investigate this correlation.

Piezoresistive digital pressure sensors (Tekscan, Inc., South Boston, MA, USA) are one of the newer available technologies for quantification of compressive loads and contact pressures. These thin-film sensors consists of a matrix of rows and columns of a patented semi-conductive ink coating that changes its electrical resistance when force is applied to it. These rows and columns intersect to form sensing elements (*sensels*) that are sandwiched between two flexible polyester sheets. The pressure on each element is assumed to be constant and equal to the pressure measured at the centre where the piezoresistive strips cross. By electronically scanning and measuring the change in resistance at each individual sensing element, the timing, force and location of contacts on the sensor surface can be determined. Raw (uncalibrated) output can be exported as a 8-bit b/w image.

The PEMFC used for testing was designed and assembled at the CNR-ITAE Institute. It has a multiple coil flow field with two Cu endplates clamped together by means of 8×M6 steel bolts. The active area (i.e., area of the membrane electrode assembly) is about 50 cm², while the total endplate area, which includes the sealing gasket, is about 82 cm². Hence, since the active area of the sensor array is smaller than the endplate of the fuel cell, the sensor had to be placed covering only one side of the gasket frame. Experimental tests were carried out by varying the external clamping pressure step by step. This was obtained by using a calibrated torque wrench with torque values of 2, 4, 6, 8, 10 and 11 Nm. At each step, after waiting for about 30 s, the torque value on each bolt was checked to account for possible gasket or porous membrane electrode relaxations. The eight bolts were clenched using always the same sequence. Measurements were taken waiting 180 s after each step increase or decrease.

Before embedding the sensor array into the fuel cell, it was validated for accuracy and repeatability by designing a pneumatic calibration device which allows to apply uniform static pressure levels over the whole sensor area. The calibration device consists of two flat and thick metal plates (planarity tolerance $\pm 5 \mu\text{m}$). The film sensor is first placed onto the bottom plate and covered with a thin sheet of Teflon (0,010 mm). Sealing is achieved by means of a Gore-Tex gasket placed over the Teflon membrane. An air chamber was finally obtained by interposing a rigid polycarbonate frame between the two stainless steel plates, which were clamped together by 12×M10 steel bolts. The pressure into the air chamber is controlled by a pressure regulator. A SIT-certified 0,05% accuracy class digital pressure transducer (AEP Transducers, Modena, Italy), having a resolution of 0,2 kPa, was used as reference pressure meter for the static calibration. Two holes placed in the bottom plate allow the residual air to be driven out from the sensor compartment.



Preliminary results reported in this study showed that, as the clamping torque on the endplates is increased, the average pressure on the MEA remains almost constant but its distribution changes. The core area of the electrode becomes progressively more unloaded while average stresses on the gasket rise up, with significant stress concentration around the edge corners.

The obtained results were also compared to surface map contours measured by means of Digital Image Correlation and Tracking (DIC/DDIT). This is a no-contact optical measurement method that employs tracking and image registration techniques for accurate 2D and 3D measurements of displacement fields from digital images. It directly provides full-field displacements and strains by comparing the digital images of the fuel cell's end plate surface in the un-deformed (or reference) and deformed states respectively.

The proposed measurement system may assist the development of next-generation fuel cells or could be used as a powerful validation tool for detailed finite element models.

REFERENCES

- 1 W.K. Lee, C.H. Ho, J.W.V. Zee, M. Murthy, "The effects of compression and gas diffusion layers on the performance of a PEM fuel cell", *Journal of Power Sources*, vol. 84, pp. 45–51, 1999.
- 2 J. Itonen, M. Mikkola, G. Lindbergh, "Flooding of gas diffusion backing in PEFCs: physical and electrochemical characterization", *Journal of Electrochemical Society*, vol. 151, pp. 1152–1161, 2004.
- 3 H.S. Chu, C. Yeh, F. Chen, "Effects of porosity change of gas diffuser on performance of proton exchange membrane fuel cell", *Journal of Power Sources*, vol.123, pp. 1–9, 2003.
- 4 D. Chu, R. Jiang, "Performance of polymer electrolyte membrane fuel cell PEMFC stacks", *Journal of Power Sources*, vol. 83, pp. 128–133, 1999.
- 5 W.R. Chang, J.J. Hwang, F.B. Weng, S.H. Chan, "Effect of clamping pressure on the performance of a PEM fuel cell", *Journal of Power Sources*, vol. 166, pp. 149-154, 2007.
- 6 X. Wang, Y. Song, B. Zhang, "Experimental study of clamping pressure distribution in PEM fuel cells", *Journal of Power Sources*, vol. 179, pp. 305-309, 2008.
- 7 S. J. Lee, C.D. Hsu, C.H. Huang, "Analyses of the fuel cell stack assembly pressure", *Journal of Power Sources*, vol. 145, pp. 353–361, 2005.

HIGH SENSITIVITY MACH-ZEHNDER INTERFEROMETER FOR SUB-NANOLITER LIQUID SENSING

G. Testa, **R. Bernini***

IREA-CNR, Via Diocleziano 328, 80124 Napoli, Italy

L. Zeni

DII, Seconda Università di Napoli, Via Roma 29, 81031 Aversa, Italy

Yujian Huang, P. M. Sarro

ECTM-DIMES, TUDelft, NL-2600 GB Delft, The Netherlands

Abstract

Integrated Mach Zehnder interferometers are very powerful optical sensor device, able to detect low refractive index changes with very high accuracy. For this reason, new configurations, capable to enhance the optical sensitivity of these devices, are of great interest.

We report the feasibility of a high sensitivity integrated liquid core Mach-Zehnder interferometer (MZI) based on liquid core ARROW waveguides. ARROW waveguides are able to confine the light into the liquid core by high reflectivity Fabry-Perot mirror composing the waveguide claddings. By choosing the appropriate cladding materials, we have designed the waveguide to perform low loss propagation at $\lambda=635\text{nm}$ with a core refractive index of $n_c=1.33$.

The fabricated ARROW has been realized in silicon [1]. The waveguide channels forming the interferometer have been etched on the bottom silicon wafer by mask lithography. The high index contrast cladding layers thicknesses have been chosen in order to minimize the propagation loss [2]. The first cladding is composed by a titanium dioxide layer ($n_1=2.49$) with a thickness of $d_1=75.4\text{nm}$ deposited by atomic layer deposition. The second cladding is silicon dioxide layer ($n_2=1.46$) and it has been deposited by LPCVD ($d_2=262\text{nm}$). The liquid into the core was infiltrated by capillary effect (methanol, $n_c=1.32$).

Respect to conventional MZI, liquid core MZI offers the advantage to have an improved sensitivity due to the direct optical coupling of the light with the liquid sample. For this reason such a new optofluidic configuration has attracted much attention in the last few years and some examples of liquid interferometers have been recently reported [3]-[4].

An optofluidic MZI has been previously demonstrated from our group [5]. However, the asymmetric geometry induces a strong degradation of the device's performances due to the low visibility of the interferometer.

Here we demonstrate that with an accurate design of the device geometry, it is possible a great improvement of interferometer's visibility also for high asymmetric Mach-Zehnder configurations, improving in this way the sensitivity of the device [6]. The visibility of a MZI is strictly related to the polarization and the intensity balancing between the beams emerging from the two arms of the interferometer. The filtering properties of the ARROW in terms of polarization permit to get the interfering beams with the same polarization (TE) independently to input polarization [5]. Hence, to achieve a good visibility factor we modified the shape of the arms in order to balance, as well as possible, the intensity of the interfering beams. A schematic layout of the proposed device is showed in Fig.1.

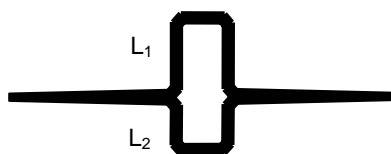


Fig.1 A schematic layout of the MZI.

The device is composed by an input straight waveguide, followed by a taper waveguide ending into a T junction that splits equally the input power into the two arms of the interferometer. Each 90°-bent waveguides composing the two arms of the MZI consists of cut-type bends. The total length of the device is 2.5 mm and the required volume is 160pl.

After propagating in the two arms (L_1 , L_2), the emerging beams accumulate a phase difference given by

$$\Delta\varphi = \frac{2\pi}{\lambda} n_{eff} (L_1 - L_2), \quad (1)$$

where n_{eff} is the effective refractive index of the core and λ is the working wavelength. Since liquid waveguides compose the device, a length difference $\Delta L=L_1-L_2$ between the two arms is required to achieve a phase delay between beams at the output. The transmitted intensity from the device is given by

$$I \propto 1 + V \cos(\Delta\varphi), \quad (2)$$

where the phase difference $\Delta\varphi$ is given by eq.(1), $V=(I_{max}-I_{min})/(I_{max}+I_{min})$ is the visibility of the interferometer. In the proposed layout, the intensity unbalance between interfering beams is only due to the different length of the straight waveguides of the arms that causes different propagation loss. By taken into account the attenuation losses of the fabricated liquid ARROWs [1], a visibility of about 99.9% is theoretically calculated with $\Delta L=100\mu\text{m}$. We have fabricated and optically characterized an optofluidic MZ interferometer with a sensing length of $\Delta L=100\mu\text{m}$. In Fig.2 the normalized transmitted spectrum is showed. From the spectrum we have calculated a visibility factor of $V=98\%$, in good agrees with the expected one. The free spectral range (FSR) measured from the spectrum around $\lambda=640\text{nm}$ is $\Delta\lambda\sim 1.49\text{nm}$, and agrees well with the theoretical one (1.55nm)

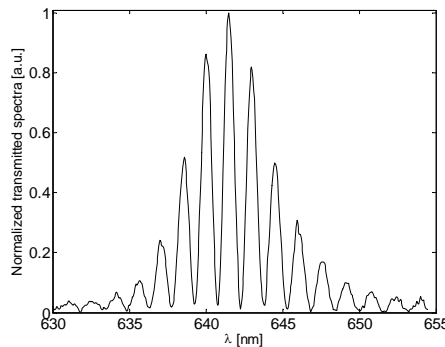


Fig.2 Measured transmitted spectrum from MZI, FSR $\Delta\lambda\sim 1.49\text{nm}$.

This MZ interferometer can be applied as high sensitivity optical sensor. If the liquid core refractive index changes, a variation of the optical output power can be detected at fixed wavelength; the estimated sensitivity is 10^{-6} RIU, around $\lambda=640\text{nm}$ and at $n_c=1.33$.

REFERENCES

1. G. Testa, Y. Huang, L. Zeni, P. M. Sarro and R. Bernini, IEEE Photon. Technol. Lett., in press, (2009).
2. R. Bernini, S. Campopiano, L. Zeni, IEEE J. Selected Topics in Quantum Elect. 8, (2002), 106.
3. P. Domachuk, C. Grillet, V. Ta'eed, E. Mägi, J. Bolger, B. J. Eggleton, L.E. Rodd and J. Cooper-White, Appl.Phys.Lett. 86, (2005), 024103.
4. P. Dumais, C. L. Callender, J. P. Noad and C. J. Ledderhof, Opt. Express, 16, (2008), 18164
5. R. Bernini, G. Testa, L. Zeni, and P. M. Sarro, Appl. Phys. Lett., 93, (2008), 011106.
6. K. Tiefenthaler and W. Lukosz, J. Opt. Soc. Am. B, 6, (1989), 209.

* **CORRESPONDING AUTHOR:** E-mail: *bernini.r@irea.cnr.it*, Ph: +39081570799, Fax: +390815705734

Fast Multi-Channel Driver for High-Voltage Micromirrors Switches

Andrea Simonetti^{1,2}, Stefano De Luca², Alessandro Trifiletti¹

1 Department of Electronic Engineering

University of Rome "La Sapienza". I-00184 Rome, ITALY

e-mail: [simonetti, trifiletti]@die.uniroma1.it

2 Evodevo S.r.l., I-00040, Pomezia, ITALY

e-mail: s.deluca@evodevo.it

Abstract

Introduction: Scanning and digital micro-mirrors are some of the most important elements of the MOEMS (Micro-Opto-Electro-Mechanical Systems) devices. Particularly, the micro-machined based switches are an attractive solution for the all-optical networks (i.e. telecommunications) such as the optical switches [1][2][3], the phase-modulation-induced switching [4] and frequency down-conversion [5]. The MOEMS switches require a square-wave excitation with a depth of modulation that may be more than one hundred volts at a frequency of repetition that is closely related to the particular device, similarly to effective tilting angle. Nonetheless, the current state-of-the-art technology demonstrates the lack of economic tools to drive the array of these actuators or the multi-axis micro-mirrors. It should be noted that the power density is also an appreciable figure-of-merit in the market context, so higher frequencies thus higher loads and higher voltages capability, requires everything else to get smaller and there is thus a greater emphasis to very advanced designs built with manufacturing processes such as surface-mount techniques. Therefore, in this work we propose a low-priced, multi-channel digital handheld drive with an advanced feedback loop that allows fast slopes with a very large voltage and high frequency span. Experimental waveforms for the proposed interface are also given to demonstrate its validity.

Basic principle: Starting on the output side and assuming a capacitive load, the proposed interface is based on a high-voltage CMOS (Complementary Metal-Oxide Semiconductor) logic port capable of a zero-return condition, where the active devices must have a low channel charge accomplished with a high voltage and high current capability. Preliminarily, a simple wired-based logic circuit makes this system less cost effective and faster than the PAL (Programmable Array Logic) or the FPGA (Field Programmable Gate Array) conventional solutions. The shift-level block is performed with a fast opto-couplers system that allows a high isolation among the logic and the power sections. In order to deal with high-frequency inputs, this block is connected as a bootstrapping circuitry to reduce signal distortion by keeping a constant gate-to-source voltage of the output coupled MOS. Additional source degeneration is also used for thermal stability. Such a topology, usually involves a turn-on and turn-off transient losses in the output stage which can be greater than its DC conduction losses. So a high-current driver for the output active devices allows a fast transient response and effectively minimizes the rise and fall times of the system. Synchronization for the complementary ground referenced MOS switches (zero return totem-pole), is obtained by processing the gate signals of the floating switches that are properly shifted also with an opto-couplers devices, with an external input signal. The logic flow, delays the starting of the zero return state after the end of the main logic state, such as the return at the normal operation is delayed at the end of the zero return condition. Since the controller is based on a completely static asynchronous state-machine, the output analog level (positive voltage, negative voltage, ground connection), can be maintained for an indefinite time. Now, considering that the zero-return overcomes the standard input signals (similarly to an enabling function), it is possible to obtain a sophisticated modulation of the micro-mirrors switches. The grounded low-impedance also prevents the breakdown voltage

on the capacitive loads, which is induced by the parasitic currents.

Experimental results: Fig.1 shows the proposed interface built on a printed circuit board using customized magnetic components and optimized layout. The output amplitude is digitally selectable, independently for each level, from 1 V_{p-p} to 250 V_{p-p} with four channels simultaneously loaded at 400 pF and 22 KOhm up to 1 MHz input frequency. The minimum slew rate is 450 V/μS in the normal operation and 1000 V/μS for the zero-return. The experimental waveforms with a 5V, 50 KHz square-wave input are shown in Fig. 2(a) and 2(b) respectively. The zero-return has been characterized by applying the same previous excitation to its port with the main input alternately forced between low and high logic levels, as shown in Fig. 2(c),(d) and in Fig. 2(e),(f) respectively.

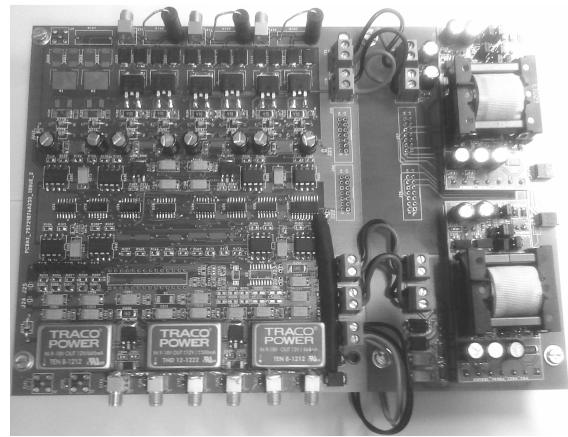


Fig. 1. The proposed drive in the four channel version. The digital inputs are 3.3 V and 5V compatible. This device is powered by an unregulated power-supply from 11V to 18V with a typical power consumption of 12 W at full load. Optional microprocessor and serial port are also provided to support a pc-based instrument.

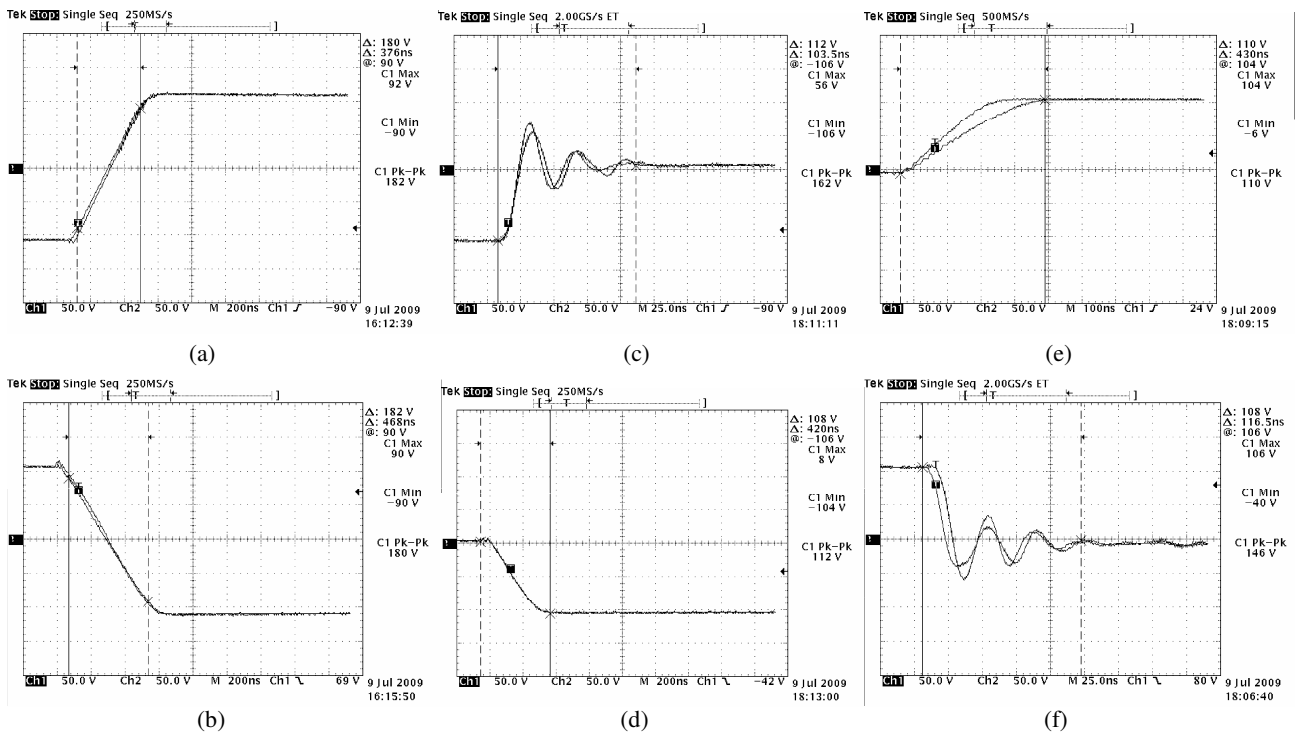


Fig.2. The output waveforms with two channels simultaneously activated. Particular of the output with the enable input set to low and the main input set from low to high (a) and high to low (b). Particular of the output with the enable input set from low (disabled) to high (c; f) and high to low (d; e) with the main input set to low (c; d) and high (e; f) respectively. Only in the fig. (c) and fig. (f) results a little overshoot smaller than 20nS. In the other cases, the settling-time is negligible.

REFERENCES

1. C.H. Kim, N. Park, Y.K. Kim, "Reflective type variable optical attenuator using off-axis misalignment," *IEEE/LEOS International Conference on Optical MEMS* (2002), pp. 55-56, 2002.
2. M.S. Yang, Y.O. Noh, Y.H. Won, W.Y.Hwang, "Very low crosstalk 1x2 digital optical switch integrated with variable optical attenuators," *Electronics Letters*, vol. 37, pp. 587-588, 2001.
3. C.R. Giles, V. Aksyuk, B. Barber, R. Ruel, L. Stulz, D. Bishop, "A silicon MEMS optical switch attenuator and its use in lightwave subsystems," *IEEE Journal on Quantum Electronics*, vol. 5, pp. 18-25, 1999.
4. D. N. Guerra, M. Imboden, P. Mohanty, "Electrostatically actuated silicon-based nanomechanical switch at room temperature," *Applied Physics Letters*, vol. 93, 033515, 2008.
5. H. B. Chan, C. Stambaugh, "Fluctuation-enhanced frequency mixing in a nonlinear micromechanical oscillator," *Physical Review B* 73, 224301, 2006.

ARTIFICIAL IMMUNE SYSTEMS: A NOVEL APPROACH TO ELECTRONIC NOSE PATTERNS CLASSIFICATION

Saverio De Vito, Girolamo Di Francia

ENEA – Sez. MATNANO – C.R. Portici, P.le E. Fermi, 1 80055 Portici (NA)

E. Martinelli, R. Di Fuccio, C. Di Natale, A. D' Amico

Department of Electronic Engineering, University of Rome “Tor Vergata”

Via del Politecnico 1, 00133 Rome, Italy

Abstract

Artificial olfaction data analysis is an active field of research gaining the attention of many pattern recognition practitioners. Several classical or ad-hoc approaches have been explored or developed for the use in signal processing (drift reduction), explorative data analysis, qualitative olfaction tasks as well as quantitative gas concentration estimation tasks. Most applications rely on the use of statistical sub-symbolic approaches ranging from simple use of linear techniques (e.g. PCA, LDA, etc.) to the use of different neural networks based architectures including SVMs [1][2].

In the last ten years a novel biomimetic approach named AIS (Artificial Immune Systems), based on mammalian immune system analogy, is being explored in different application fields both as a data clustering and pattern recognition architecture [3]. In fact, advancements in immune systems theory have explained their peculiar and rather interesting features like self/non-self recognition, i.e. the capability of identifying the presence of hostile intruders, and memory effects, i.e. the capability of retaining a memory image of the past hostile encounters exploiting it for setting up a fast and efficient immune response to future infections. Artificial immune systems are mainly based on the exploitation of these features in order to build a biomimetic approach for instance based pattern recognition with tuning capabilities for the plasticity / stability trade-off.

Actually, mammalian immune systems theory is based on the concept of an innate immune response embedded in an immune memory cells set. This set evolves in time while immune cells come in touch with different potentially pathogenic intruders, gaining and retaining a “knowledge” of the intrusion that will be useful for setting up a faster, massive response for future encounters. This recognition/evolution/memory framework is characterized by the antibody/antigen binding relationship: basically B class lymphocytes cells carry multiple molecular receptors (i.e. the antibody) that bind with peculiar molecular loci on foreign pathogenic materials recognizing it by molecular complementarity. These binding events trigger the multiplication of the recognizing B cell (clonal expansion); after the infection, part of these mature cells (clonal selection) are retained in the body building up the immune system “memory” capability.

Here, we explore the possibility to use of AIS for artificial olfaction data analysis while introducing it to the AO community. One of the most recent supervised AIS algorithm is AIRS (Artificial Immune Recognition System) based on an idea originally developed by Watkins and Timmis in 2002 [4]. In AIRS approach, a preliminary memory cells set characterized by their antibodies is generated including randomly chosen antigens (training) samples; actually, antibody and antigens are encoded as vectors whose dimensions are equal to data feature space dimensions. Memory cells are then tagged with a particular dataset class so to become one possible representative sample for this particular class. *Affinity* (computed as vector Euclidean distance) is a key ideas for AIRS. Dataset items (antigens) are at this point, *presented* to the memory set; memory cells tagged with the presented antigen class that show a low affinity value with it, are selected to be cloned. Even memory cells that are tagged with a different a class label simultaneously retaining high affinity value with the presented antigen undergoes clonal expansion. The number of generated clones is controlled with relative affinity. Afterwise, clones undergo a maturation process introducing random mutations. Candidate memory cells showing smaller antigen affinity or expressing sufficient difference with the antigen vector, if tagged with a different class, are selected to be

cloned again while the remaining set is discarded. Several cloning/pruning cycles are carried out until a stop condition is reached. The process encompass all training set samples. At the very end of the process, a compact memory set embedding the immune system knowledge about the training set classes has been developed. A KNN algorithm is then applied to reach the classification of unseen samples.

In this work, we compare the results obtained by a properly trained AIRSv2 algorithm with a classic BPNN approach on a publicly available dataset (Coffee blends, PCA based dataset [5]) at different training/test set partition percentage. The dataset is characterized by 5 sensors steady state readout of the pico-nose response to coffee samples belonging to 7 different blends. Best results are pursued by exploring AIRS, as well as BPNN, parameter space with a brute force approach, i.e. for each partition percentage, a multidimensional matrix of possible parametric setup is explored for obtaining best performance for the two classifier. For each point in the selected parameter space, 30 training runs have been performed with different random choice of training and test samples and classification performance on test set have been averaged in order to tackle statistical performance variability of the overall model. At each partition, AIRS and NN classification best results have been computed by using WEKA framework (see [6]) and compared while differences have been checked for statistical significance at 95% confidence level. Results reported in table 1 show that the generalization performance obtained with the artificial immune system approach are quite comparable with those of one of the best performing statistical classifier used in artificial olfaction community. NN approach retain a slight advantage as regards as classification results but a deeper analysis of the same results shows how this difference cannot be deemed as significant from the statistical point of view. Here, it is worth to note that generally AIS approaches have been investigated and tuned only for a few years with respect to the well established neural framework and hence are expected to significantly improve their performance figures.

We believe that AIS carry significant novelty features both for the preliminary data analysis point of view (clustering, data compression, class related characteristic pattern identification etc.) and from classification point of view. Furthermore they express improved output readability with respect to classical statistical pattern recognition approaches (e.g. neural networks) while having the potential to efficiently represent an evolving knowledge about sensor response that could be potentially exploited for drift effects mitigation.

Table 1. Performance comparison between AIRS and BPNN classifiers at different training/test set partition percentage. For AIRS, 50 different parameter setup have been explored with a total of 50*30*6=9000 training runs. Average correct classification percentages of best performing classifier setup together with computed standard deviations are reported.

Training set Percentage	Best AIRS Result	Best NN Result
10	65.29 (3.77)	69.50(7.95)
25	78.52 (3.32)	86.29(3.75)
35	81.74 (2.79)	88.86(3.27)
50	84.05(2.57)	91.01(2.41)
75	87.42(3.59)	92.93(2.75)
90	88.99(5.45)	94.02(6.03)

REFERENCES

1. A. Hierlemann, R. Gutierrez-Osuna, "Higher-order Chemical Sensing", Chemical Reviews, 2008, 108, 563-613.
2. S. De Vito et al., Gas concentration estimation in ternary mixtures with room temperature operating sensors using tapped delay architectures, Sensors and Actuators B Chem. 124, 309-316 (2007)
3. L.N. de Castro and J. Timmis, Artificial Immune Systems: A New Computational Intelligence Approach (2002). Springer, London.
4. A. Watkins et al., Artificial Immune Recognition System (AIRS): An Immune-Inspired Supervised Learning Algorithm. Genetic Programming and Evolvable Machines, 5 (3): 291-317, September 2004
5. M. Pardo and G. Sberveglieri, Coffee analysis with an electronic nose, IEEE Trans. Instrum. Meas. **51** (2002), pp. 1334-1339
6. Mark Hall et al., The WEKA Data Mining Software: An Update; SIGKDD Explorations, Volume 11, Issue 1 (2009).